Microstructural Evolution of 11Al-3Mg-Zn Ternary Alloy-Coated Steels During Austenitization Heat Treatment

JUN-KAI CHANG and CHAO-SUNG LIN

This study details the microstructural evolution of a commercial hot-dip 11Al-3Mg-Zn-coated steel during austenitization. After 5 minutes of austenitization at 1173 K (900 °C), the ternary alloy coating transformed to consist of a nearly pure Zn as the major layer, a Fe-Al alloy layer at the interface, and a thin oxide overlay. The Fe-Al alloy layer effectively acted as the inhibition layer to prevent Fe from diffusing and reacting with Zn, which in turn retained the molten Zn layer and the integrity of the surface oxide layer. Moreover, the potential difference between the 11Al-3Mg-Zn coating and the steel substrate remained similar after austenitization, signifying the resulting coating kept its sacrificial protection capability.

DOI: 10.1007/s11661-017-4126-6

I. INTRODUCTION

WEIGHT reduction is one of the main trends in the automobile industry to reduce fuel consumption and carbon dioxide emission. Advanced high-strength steels (AHSS) have thus been widely used in body in white, which also enhances the passengers' safety and crashworthiness.[1,2] Conventional cold-forming technology for the AHSS, however, has some disadvantages of springbacks and wrinkles because of their high strength.[3] The hot stamping process provides excellent formability.[3–5] Nevertheless, oxidation and decarburization that appear during austenitizaton are associated with the hot stamping process.[4,6] Oxidation-preventive oils have been developed for press-hardening steel without providing additional corrosion protection capability for automotive parts.[7] Surface coatings are thus a necessity for press-hardening steel, including hot-dip aluminizing, hot-dip galvanizing (GI) and galvannealing (GA), and electrogalvanizing Zn-Ni coating.[6,8,9] Among them, hot-dip aluminizing and galvanizing have been commercialized, such as Usibor AluSi, GI, and GA press-hardening steels.[10]

Hot-dip aluminizing is the technology most widely employed for press-hardening steel.[9,11–15] Hot-dip aluminized coatings are sufficient to solve the oxidation and decarburization problem *via* the formation of a compact Al_2O_3 layer.[9,11,13,15,16] The resulting Fe-Al alloy layer offers good barrier protection, but it is not enough to withstand harsh environments because of the insufficient sacrificial protection.[17,18]

Hot-dip galvanized coatings are generally recognized for providing both the barrier protection and the sacrificial protection on steels.[6,19,20] When a hot-dip galvanized steel is subjected to austenitizaton, Zn-saturated α-Fe (α-Fe(Zn)) and liquid Zn with an Fe content generally lower than approximately 10 wt pct coexist in the alloy coating layer.[6,21–24] When forming is in progress, the liquid Zn(Fe) penetrates the steel substrate and cracking occurs along α-Fe(Zn) grain boundaries and proceeds down to the steel substrate.[21,22] This is called "liquid metal-induced embrittlement (LMIE),"[6,21,22,25,26] which markedly deteriorates the formability of steels. Upon cooling, liquid Zn(Fe) and α-Fe(Zn) react to form the Γ phase by a peritectic reaction occurring at 1055 K (782 °C). The resulting diffusion layer after hot stamping is thus composed of the α-Fe(Zn) and Γ. Because the α-Fe(Zn) and the Γ phase have a nobler corrosion potential and less corrosion current density compared with the pure Zn coating,[27,28] the phase transformation of the coating during hot stamping has a direct and, to some extent, positive effect on the corrosion resistance of the press-hardening steel parts. Dosdat *et al.* compared the corrosion resistance of press-hardened boron steels with Al-10 wt pct Si, GI, and GA coatings with a hot-dip galvanized interstitial-free (IF) steel for cold stamping as the reference.[10,17] For painted samples, the press-hardened GI and GA steels exhibited better cosmetic corrosion and cut-edge corrosion resistance than did the press-hardened Al-10 wt pct Si steel and GI IF steel after 10 weeks of the VDA 621-415 test. The resulting

JUN-KAI CHANG and CHAO-SUNG LIN are with the Department of Materials Science and Engineering, National Taiwan University, 1, Roosevelt Road, Section 4, Taipei 106, Taiwan. Contact e-mail: csclin@ntu.edu.tw
Manuscript submitted December 28, 2016.
Article published online May 17, 2017

α-Fe(Zn) and Γ diffusion layer not only affords cathodic protection but also enhances the corrosion resistance resulting from an increase in the thickness and in the corrosion potential after being alloyed with more Fe, as well as a decrease in the potential difference between the diffusion layer and the steel substrate. Nevertheless, the GI IF steel had the smallest maximal pitting depth in scribe lines among the various painted steels. Moreover, white rusts were observed on the GI IF steel during early stages of corrosion, but red rusting prevailed for all press-hardened steels in the beginning of corrosion. As a result, the cathodic protection in distance can be lower for the press-hardened GI and GA steels compared with the GI IF steel.[28]

Several kinds of Zn-Al-Mg coated steels have been studied, with emphasis on the corrosion resistance.[29–34] The corrosion resistance has been improved by the formation of Mg-species-containing corrosion products, which are more chemically stable than the corrosion products found in Zn coatings.[29] Moreover, crevice corrosion is retarded in Zn-Al-Mg coated steels compared with GI steels.[32] 11Al-3Mg-Zn coating, known as Superdyma®, is fabricated by the Nippon Steel Corporation, Japan.[31,33] Superdyma coatings on steel sheets have been shown to have excellent long-term corrosion resistance in constructional applications.[31,33] Zn-Al-Mg coatings have thus been used in twinning-induced plasticity steels for the automobile industry because of their excellent corrosion resistance.[10,30,32]

The phase evolution of Zn-coated steels during austenization has been extensively studied, including GI, GA, and Galvalume (55 wt pct Al-Zn)® coatings.[21–23,27,35–38] Nevertheless, knowledge of the phase transformation of Zn-Al-Mg coatings during hot stamping is still absent. How to design the Zn-based coating for press-hardening steel is an important topic in the automobile industry. The remnant Zn present in the α-Fe or as Zn-rich phases is essential to provide sufficient sacrificial protection for hot-stamped steel parts, specifically those with wide scribes. In this study, the microstructural evolution of 11Al-3Mg-Zn coatings on steel sheets during austenitizaton was studied. The electrochemical analysis was employed to study the relation among the phase transformation, corrosion resistance, and sacrificial protection.

II. EXPERIMENTAL PROCEDURE

A. *Materials*

Commercial hot-dip 11Al-3Mg-Zn-coated steel sheets produced by the Nippon Steel Corporation, Japan, were employed for this study. The coating is Superdyma® K27 that stands for a nominal coating mass of 270 g/m^2 for each side. Table I shows the nominal composition and thickness of the steel substrate.

To simulate the austenitization process in hot stamping, the as-received, hot-dip galvanized steels were cut into dimensions of 20 mm × 100 mm and heated to 1173 K (900 °C) with a heating rate of approximately 20 K/s under the ambient atmosphere. After isothermal holding at 1173 K (900 °C) for 5 minutes, the panels were withdrawn and placed on a cast iron block, which had been sprayed with liquid nitrogen, to simulate the rapid cooing in hot stamping.

B. *Microstructural Characterization*

X-ray diffraction (XRD, Rigaku TTRAX 3) was employed to identify the phases of the hot-dip 11Al-3Mg-Zn-coated steel sheet before and after austenitization using monochromatic Cu-K_α (λ = 1.54439 Å) radiation at 30 kV and 50 mA. The scanning speed was set to be 4 deg/min. Field-emission gun scanning electron microscopy (FEG-SEM, Nova Nano SEM 450) was used to investigate the cross section of the various steel panels. The cross section was investigated under the backscattered electron (BSE) mode at 25 kV to identify the various phases. The chemical composition of the coating and the corrosion products were analyzed using the energy-dispersive spectrometry (EDS) equipped in the FEG-SEM. An electron probe X-ray microanalyzer (EPMA, JEOL JXA-8200) was also used to analyze the chemical composition distribution of the coating by mapping at 15 kV and 5×10^{-8} A.

The cross-section TEM specimen was prepared from the panel using a focus ion beam (FIB, FEI Helios 600i). The oxide layer was identified with a field-emission transmission electron microscopy (FE-TEM, FEI Tecnai G^2 F20) operating at 200 kV, with the composition measured by the EDS equipped in the FE-TEM.

An X-ray photoelectron spectroscope (XPS, A VG Thermo K-Alpha) with an Al K_α monochromatic X-ray source was used for studying the surface oxide layer. A depth profile was obtained using argon (Ar^+) sputtering with an etching rate of approximately 0.11 nm/s at an etching area of 2 × 1 mm^2 and a total depth of approximately 200 nm was recorded. The Avantage 4.16 software was employed to analyze the characteristic peaks, and the binding energy of each species was referred to the NIST database.[39]

C. *Electrochemical Measurement*

The corrosion behavior of the various steel panels was evaluated using an electrochemical stripping method. The electrochemical stripping was conducted *via* a

Table I. Detailed Information of the Coated Steel

Steel Specification	NSDCC						
Chemical Element	Fe	C	Si	Mn	P	S	Thickness (mm)
Contain (wt pct)	bal.	0.04	0.01	0.18	0.01	0.01	0.4 ± 0.02

PARSTAT 4000 using a conventional three-electrode cell. The test solution was aerated in 4 wt pct HCl solution at 298 K (25 °C). The working electrode was the steel with an exposure area of around 1.77 cm^2. A platinum plate of 16 cm^2 and a saturated calomel electrode (SCE) were used as the counter and reference electrodes, respectively.

III. RESULTS

Figure 1(a) shows the XRD pattern of the as-received, hot-dip, 11Al-3Mg-Zn-coated steel. Diffraction peaks associated with the Al, Zn, and $MgZn_2$ phases were identified based on the standard JCPDs cards. The thickness of the as-received coating was approximately 25 μm, as shown in Figure 1(b). Under the SEM/BSE mode, three distinct regions were revealed resulting from the difference in the atomic weight of the elements, including gray bulk, gray network, and white matrix. The EPMA element distribution results (Figures 1(c) through (f)) further showed that Al was detected mainly at the gray bulk areas, which is the primary phase solidified from a molten Zn-11Al-3Mg bath.[31] $MgZn_2$ was found mainly in the gray network areas, where the Al signal was relatively low. Moreover, the white matrix

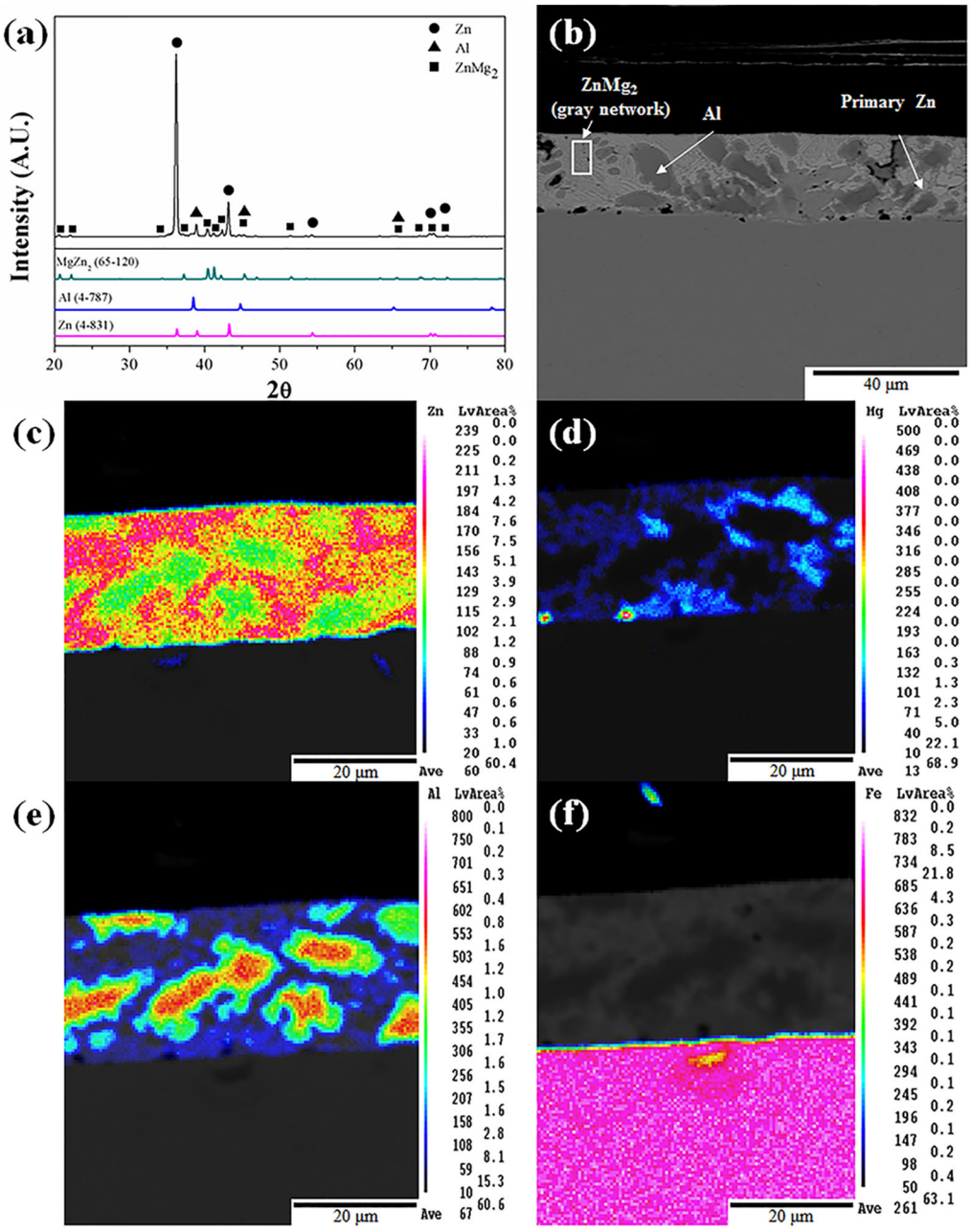

Fig. 1—(*a*) XRD pattern, (*b*) cross-sectional SEM micrograph, and EPMA element distribution of (*c*) Zn, (*d*) Mg, (*e*) Al, and (*f*) Fe of the as-received 11Al-3Mg-Zn coating.

was mainly composed of Zn. This is consistent with the results produced by Honda *et al.*[31] and Yu *et al.*[33] who reported that the network structure solidified from a molten Zn-11Al-3Mg is $MgZn_2$. Honda *et al.* integrated the results of thermal-calc computations and experiments and found that the stable phase in the Zn-rich corner of the Zn-Mg binary phase diagram is Mg_2Zn_{11}, but $MgZn_2$, a metastable phase, is present in the coating instead of Mg_2Zn_{11}.[30] The solidification path is thus revised by taking into account the effect of rapid cooling on the distinctive nucleation of $MgZn_2$ and Mg_2Zn_{11}.[31] The Al + $MgZn_2$ eutectic reaction is followed by the Al + $MgZn_2$ + Zn ternary eutectic reaction at 609 K (336 °C). Finally, the primary Al and eutectic Al decompose into monotectoid Al and monotectoid Zn at temperatures below 550 K (277 °C). As a result, the 11Al-3Mg-Zn coating is composed of an Al solid solution, a Zn solid solution, and an $MgZn_2$ intermetallic phase. The solidification sequence and microstructure relationship have also been seen in other Zn-Al-Mg coatings.[30,32–34]

Figures 2(a) and (b) are, respectively, the XRD pattern and the cross-sectional SEM micrograph of the 11Al-3Mg-Zn coating after 5 minutes of austenitization at 1173 K (900 °C). Table II is the EDS element analysis of the corresponding point in Figure 2(b).

The XRD results showed that the coating had transformed into Zn, $Fe_2Al_5Zn_X$, and oxides (ZnO and MgO) after austenitization. Moreover, the reaction between the coating and the steel substrate caused a marked change in the microstructure and thickness of the alloy layer, as shown by comparing Figure 2(b) with Figure 1(b). Specifically, (1) a continuous, polygonal crystal layer was observed at the interface. The EDS analysis (marked as ① in Figure 2(b) and Table II) showed the polygonal crystal made up of Fe and Al as a major part with Zn as a minor part, which was assigned as the $Fe_2Al_5Zn_x$ seen in the XRD pattern. (2) Large equiaxial grains were observed as the major layer of the coating and contained Zn with Fe as solid solution (EDS taken at ② in Figure 2(b)), which can be considered to be the pure Zn phase seen in the XRD pattern. EDS taken at the grain boundaries of Zn (③ in Figure 2(b)) has the similar result in ② with some Mg detected. (3) A thin oxide layer was observed on the surface of the coating.

Figure 3 shows the EPMA mapping of the coating shown in Figure 2(b). A Fe-Al alloy layer was observed at the interface between the coating layer and the steel substrate followed by a Zn layer as the major layer. Mg was found to reside along the boundaries between Zn grains. A thin oxide layer was observed on the top of the coating. The Al in the coating apparently reacts with Fe to form the Fe-Al phase, which effectively blocks the Fe from reacting with Zn. As a result, nearly pure Zn is retained in the alloy coating layer.

XPS and cross-sectional TEM were employed to characterize the detailed microstructure of the surface oxide layer. Figure 4 is the XPS depth profile from the surface to approximately 200 nm down to the alloy coating layer. Approximately 40 wt pct O was detected up to the depth of 200 nm. Moreover, Mg, Zn, and Al were the major metallic species in this surface layer, with the atomic percentage of around 45, 10, and 5 pct, respectively. Figure 5 shows the high-resolution spectra of Al2p, Mg2p, and Zn2p recorded at the depth of 90 nm from the surface. Moreover, the spectrum of each element was deconvoluted using the procedure of

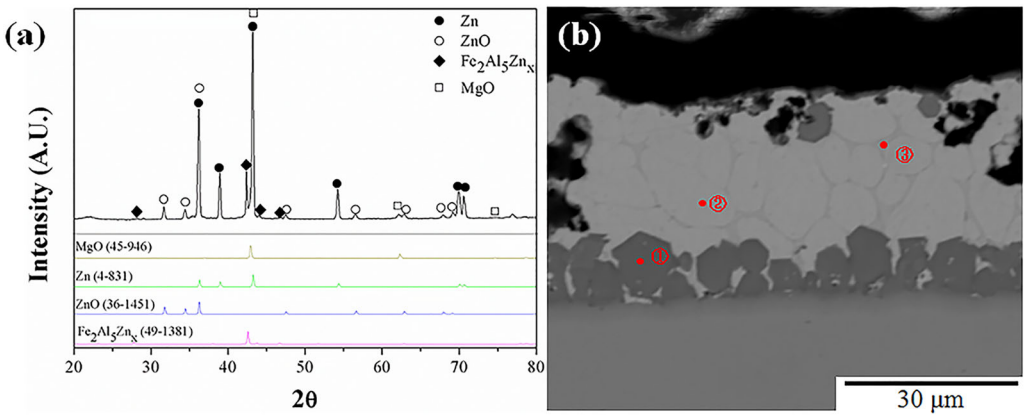

Fig. 2—(*a*) XRD pattern and (*b*) cross-sectional SEM micrograph of the 11Al-3Mg-Zn coating after 5 min of austenitization at 1173 K (900 °C).

Table II. EDS Element Analysis Result in the Corresponding Point in Fig. 2

	Element Content (Wt Pct)			
Point in Fig. 2	Zn	Mg	Al	Fe
①	15.85	—	42.75	41.4
②	99.41	—	—	0.59
③	96.29	2.27	—	1.44

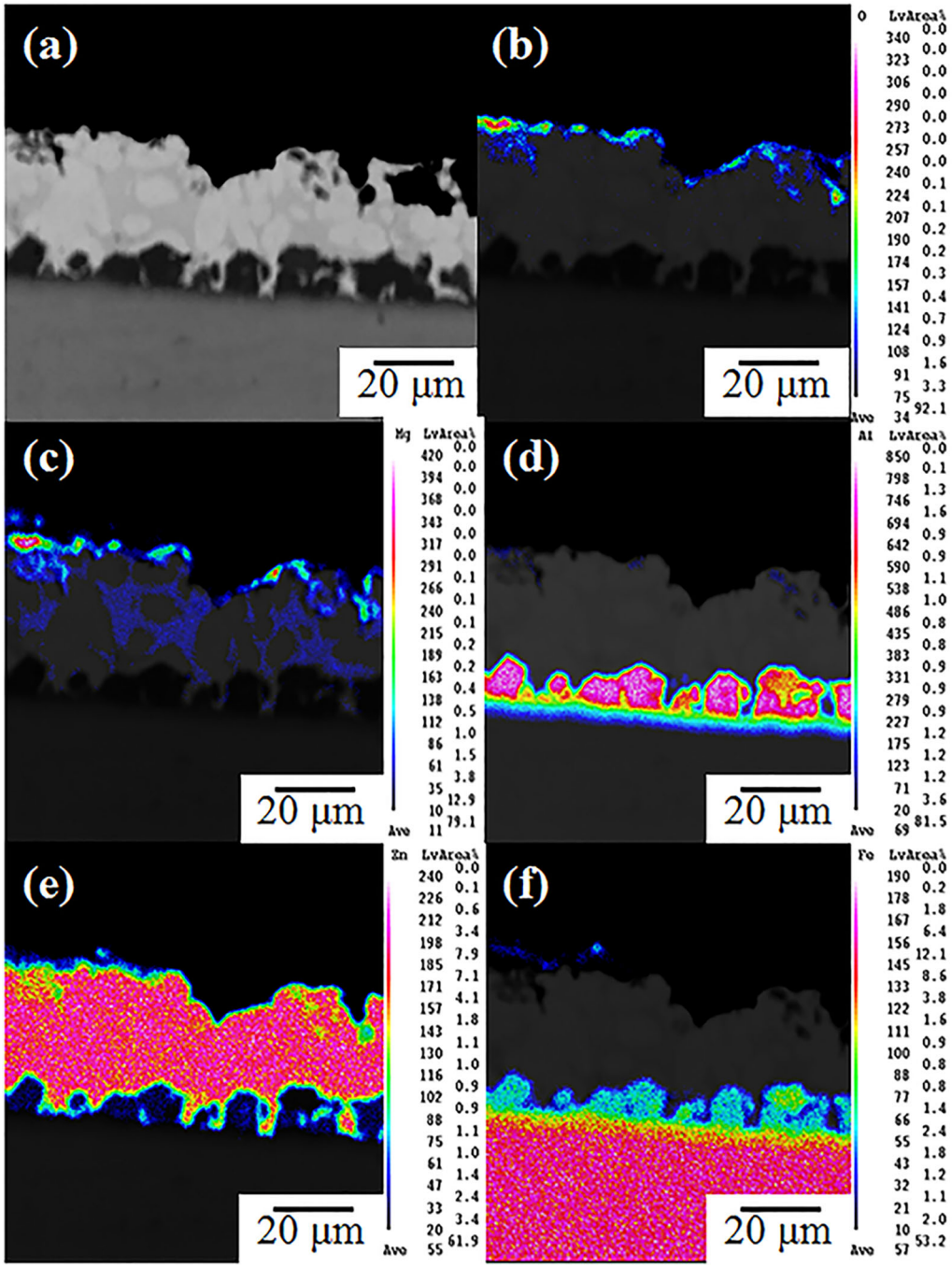

Fig. 3—(*a*) Cross-sectional SEM micrograph and EPMA element distribution of (*b*) O, (*c*) Mg, (*d*) Al, (*e*) Zn, and (*f*) Fe of the 11Al-3Mg-Zn coating after 5 min of austenitization at 1173 K (900 °C).

de-background and peaks fitting for a chosen binding energy range using the Avantage 4.16 software. The charging effect was regulated by the C1s peak at 284.6 eV as the standard for all samples,[40] and all peaks were assigned based on the NIST database and the results in the literature.[39] Two deconvoluted curves were found for the Mg2p spectrum (Figure 5(a)), including the peaks at 50.80 and 49.80 eV that can be assigned for MgO and $MgAl_2O_4$, respectively.[41–43] Meanwhile, two well-defined peaks were recorded for the Zn2p spectrum. The peak appearing at 1021.6 eV can arise from metallic Zn or ZnO.[44,45] Because the XRD diffraction peaks resulting from ZnO were detected (Figure 2(a)), the peak appearing at 1021.6 eV was primarily associated with the presence of ZnO. The 1044.70-eV peak was likely to result from $ZnAl_2O_4$[46] because the surface oxide mainly consisted of O, Mg, Zn, and Al species (Figure 4). Finally, two peaks and one shoulder were recorded for the Al2p spectrum, as shown in Figure 5(c). The peak appearing around 72.86 eV was associated

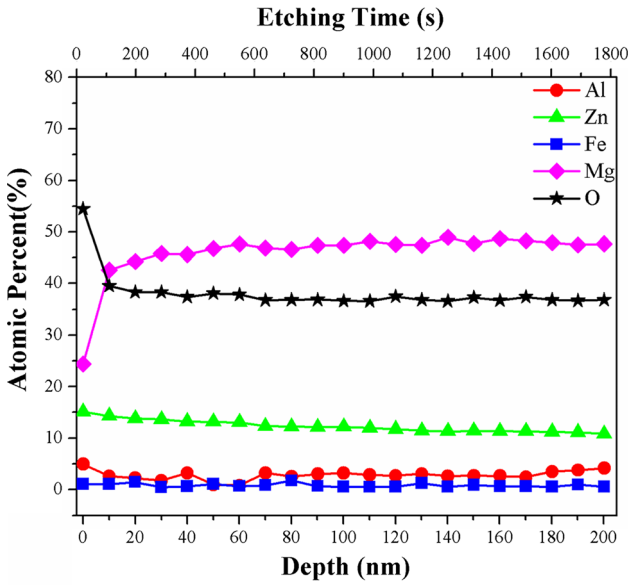

Fig. 4—XPS depth profile of the 11Al-3Mg-Zn coating after 5 min of austenitization at 1173 K (900 °C).

with the metallic Al.[47] The other peak and the shoulder can be deconvoluted to consist of two curves with a peak at 74.33 eV and 75.53 eV, respectively. The peak at 74.33 eV was likely to arise from Al_2O_3[48] and $MgAl_2O_4$,[49] whereas that at 75.53 was assigned as Al_xO, which is commonly seen in the Al oxides grown on an Al thin film.[50] The XPS depth profile and high-resolution spectrum results indicate that the oxides on the top surface were composed of MgO and ZnO, as well as of $MgAl_2O_4$, $ZnAl_2O_4$, Al_xO, and Al as the minor phases.

Figure 6 shows the TEM bright field image of the cross section around the surface of the alloy coating layer. Figure 7 shows the EDS line scan across the surface oxide layer. The oxide layer exhibited a two-layered structure. The outer layer was relatively porous; however, the inner layer contacting the nearly pure Zn layer was relatively compact. Zn and Mg species distributed rather uniformly in the oxide layer. Conversely, Al was absent in the outer layer and mainly distributed in the inner layer. Figure 7(b) also shows that Fe was not detected in the oxide layer.

The major alloy elements in 22MnB5 steel are 0.2 wt pct C, 1.15 wt pct Mn, and 0.002 wt pct B.[21,22,26,36–38] Accordingly, the major difference in the alloy composition of the steel used in this study and the 22MnB5 steel is Mn, C, and B. Lee *et al.* found that the Mn in the steels has an effect on the composition of the oxidation layer, *i.e.*, the presence of Mn_3O_4 in the ZnO layer.[38] This is because the molten Zn bath generally contains Mn dissolved from the steel substrates during galvanizing. Nevertheless, the alloy elements of the 22MnB5 steel have little influence on the phase transformation of the coating during austenitization because Mn, C, and B are not detected in the alloy layer of austenitized GI, GA, and Galvalume (55 wt pct Al-Zn)® steels.[21–23,27,36–38]

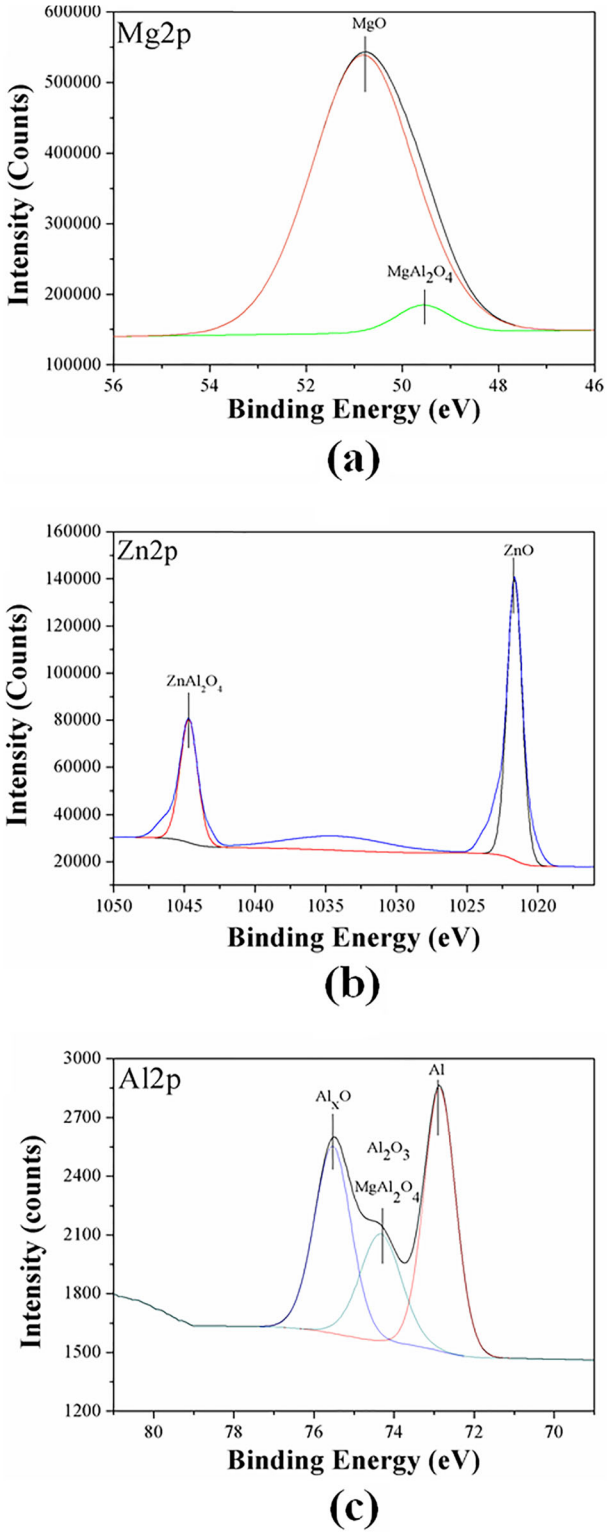

Fig. 5—High-resolution XPS spectrums of the 11Al-3Mg-Zn coating after 5 min of austenitization at 1173 K (900 °C): (*a*) Mg2p, (*b*) Zn2p, and (*c*) Al2p at 90 nm in depth.

Electrochemical stripping was used to evaluate the difference in the corrosion potential between the coating and the substrate. Figure 8 shows the potential *vs* time

plot of the 11Al-3Mg-Zn coating before and after 5 minutes of austenitization at 1173 K (900 °C). For the as-received coating, the initial potential was –1.05 $V_{SCE.}$ The potential kept at around –1.05 V_{SCE} for approximately 2450 seconds. Then, the potential rose rapidly up to –0.49 V_{SCE}, which corresponded to the exposure of the steel substrate. As for the coating after austenitization, an initial potential plateau appearing at –1.02 V_{SCE} was recorded and lasted for around 250 seconds. The potential then increased sharply, followed by a less obvious plateau at approximately –0.73 V_{SCE}, which was assumed to be associated with the exposure of the Fe-Al layer. Finally, the potential reached a stable value of around –0.49 V_{SCE} when the alloy coating layer had been totally removed. The difference between the corrosion potential between the coating and the steel substrate was here defined as the difference between the initial and final potential plateaus and was 0.563 V_{SCE} and 0.548 V_{SCE} for the as-received and austenitized 11Al-3Mg-Zn-coated steel, respectively.

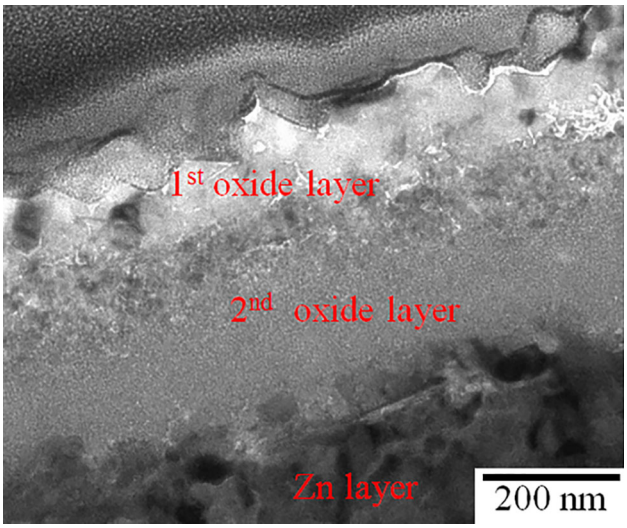

Fig. 6—Cross-sectional TEM micrograph showing the microstructure of the oxide layer on the 11Al-3Mg-Zn coating after 5 min of austenitization at 1173 K (900 °C).

IV. DISCUSSION

Two worth-noting points are found in the phase transformation of 11Al-3Mg-Zn coating during the austenitizaton process. First, the interaction between

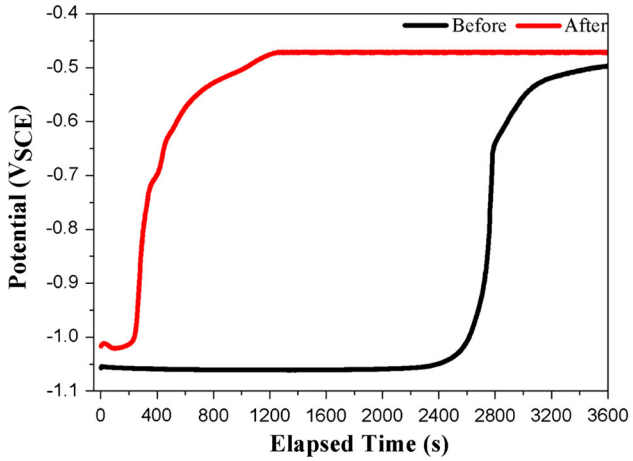

Fig. 8—Electrochemical stripping result of the 11Al-3Mg-Zn coating before and after 5 min of austenitization at 1173 K (900 °C).

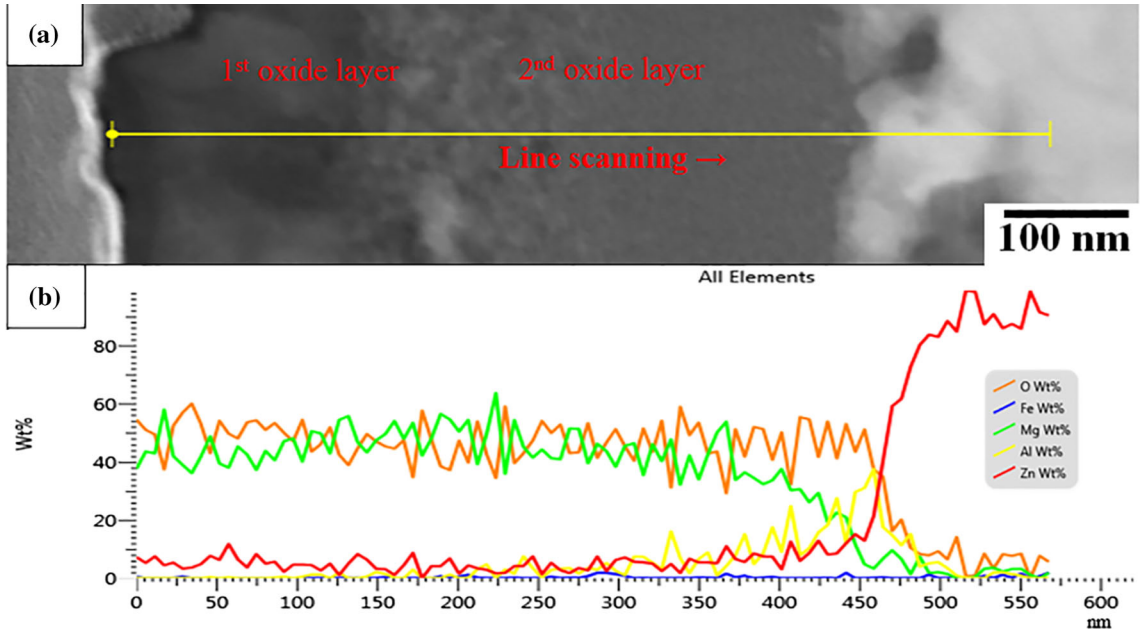

Fig. 7—(*a*) High-angle annular dark-field image and (*b*) EDS line scan of the oxide on the 11Al-3Mg-Zn coating after 5 min of austenitization at 1173 K (900 °C).

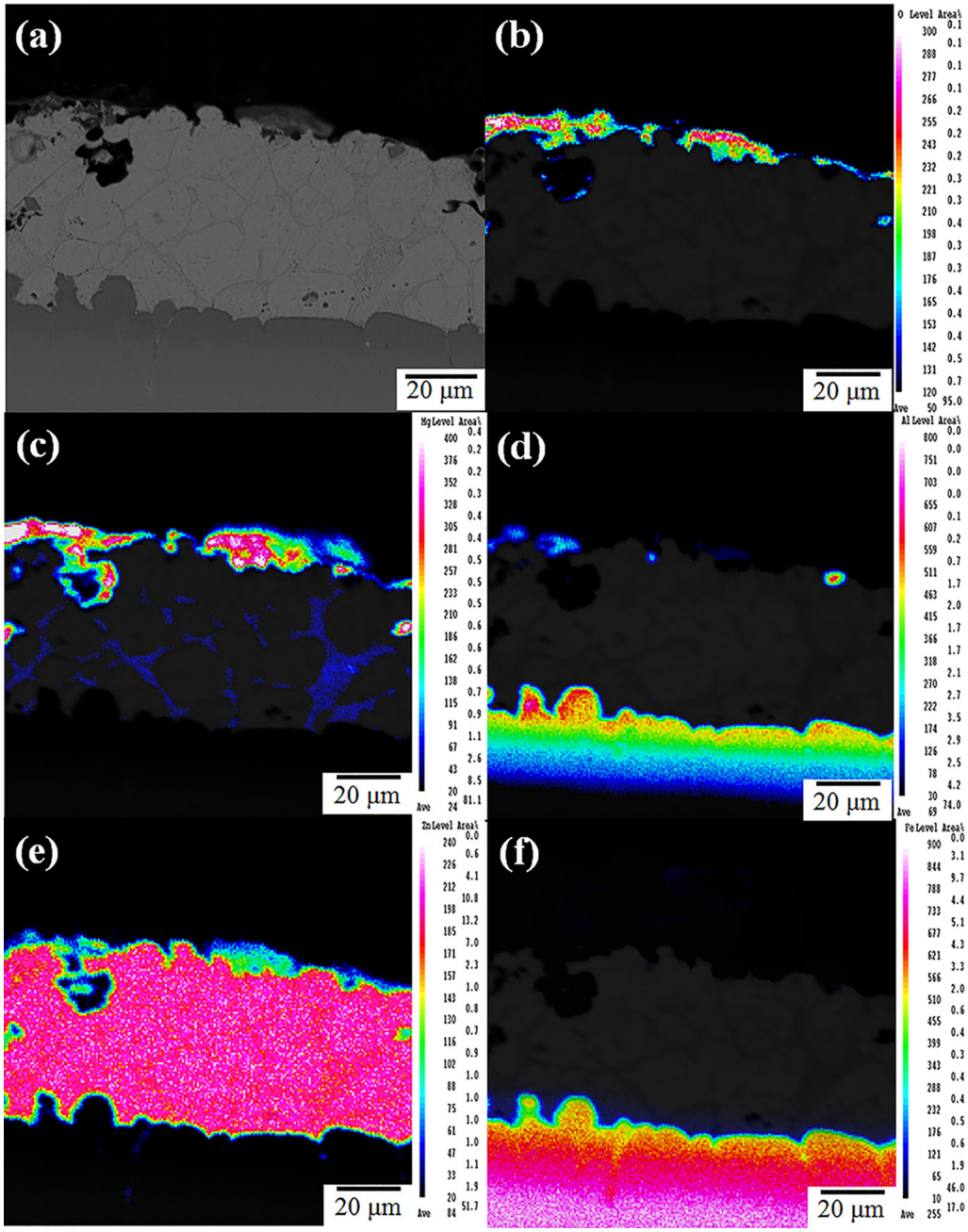

Fig. 9—(*a*) Cross-sectional SEM micrograph and EPMA element distribution of (*b*) O, (*c*) Mg, (*d*) Al, (*e*) Zn, and (*f*) Fe of the 11Al-3Mg-Zn coating after 3 min of austenitization at 1223 K (950 °C).

Fe and Al is more reactive than that between Fe and Zn; therefore, Fe and Al interacts to form the Fe-Al phases at the coating-steel interface in the absence of Fe-Zn phases. Lee *et al.*[36] employed the Factsage equilibrium thermodynamics computational software to predict the intermetallic compounds present at the 1173 K (900 °C) isothermal section of Zn-Al-Fe ternary alloy and found that the thermodynamically stable phases are a series of Fe-Al intermetallic compounds, liquid Zn, liquid Al, and α-Fe. These predicted results agree well with the thermodynamically stable phases in the Zn-rich corner of Zn-Al-Fe ternary alloy at 1173 K (900 °C).[51,52] The higher reactivity between Fe and Al also reflects the fact that around 0.12 to 0.2 wt pct of Al is generally added in the hot-dip galvanized Zn bath to slow down the Fe-Zn alloy reaction by the formation of a Fe-Al inhibition layer.[53–55] Second, Zn is largely retained after austenitizaton as it is repelled when Fe reacts with Al to form the Fe-Al alloy layer. This is unlike the results commonly seen in the literature showing that almost all of the Zn in the commercial hot-dip galvanized steel is consumed by being dissolved in the α-Fe matrix, oxidized to form Zn oxides on the surface, or alloyed with Fe to form the Γ phase.[23,38]

A side experiment was further performed to study the stability of the Fe-Al alloy layer at higher temperatures. Figure 9 shows the cross-sectional SEM micrograph and EPMA mapping results of the 11Al-3Mg-Zn-coated steel after isothermal holding at 1223 K (950 °C) for 3 minutes. An approximately 40-μm-thick Zn layer was retained, and an alloy layer composed of Fe-Al phases was still present at the coating-steel interface. The alloy layer consisted of a continuous Fe-Al layer with an average composition of 89.35 wt pct Fe, 9.88 wt pct Al, and 0.77 wt pct Zn. Individual polygonal $Fe_2Al_5Zn_x$ grains were also observed on top of the continuous Fe-Al layer and had an average composition of 65.76 wt pct Fe, 31.47 wt pct Al, and 2.77 wt pct Zn. The alloy layer had a morphology different from the polygonal $Fe_2Al_5Zn_x$ grains of the alloy layer formed at 1173 K (900 °C) for 5 minutes. It is apparent that a relatively thick Zn layer can be preserved once the Fe-Al alloy layer remains at the interface.

The Zn layer preserved in the 11Al-3Mg-Zn coating after 5 minutes of austenitizaton at 1173 K (900 °C) solidifies into relatively large Zn grains and eutectic $MgZn_2$ residing at the Zn grain boundaries. The molten Zn(Mg) is apparently protected from oxidation by the surface oxide layer with MgO as the major phase. The formation energy of MgO and Al_2O_3 at 1173 K (900 °C) is –958.88 and –1303.86 kJ/mol, respectively, which is lower than that of ZnO, *i.e.*, –455.9 kJ/mol.[56] As a result, the alloying elements in the 11Al-3Mg-Zn melt are preferentially oxidized on the surface. Moreover, MgO and Al_2O_3 have higher melting points and lower vapor pressures at 1173 K (900 °C) than ZnO.[56] The MgO-rich surface oxide layer is thus more efficient to prevent the molten Zn from oxidization and evaporation during austenitization. Zn is thus largely retained after 5 minutes of austenitizaton at 1173 K (900 °C).

It has been shown that the Al oxide formed on the surface of GI steel during austenitization can prevent the coating from further oxidation.[6,23,38] However, the Al oxide layer breaks down when the molten Zn is consumed by alloying with Fe to form various Fe-Zn intermetallic compounds during heating up and isothermal holding at austenitization temperatures.[23,38] The protectiveness of Al oxides is then lost, signifying that the presence of Zn melt itself is a prerequisite for the prevention of severe oxidation. Consequently, the presence of Mg and Al in a ternary Zn-Al-Mg coating provides a synergetic effect for reduced oxidation during austenitization: (1) Most Al reacts with the steel substrate to form a stable FeAl alloy layer to avoid the development of the various FeZn intermetallic compounds. (2) Mg contributes to the formation of a more stable oxide layer as most Al have been consumed during the formation of the FeAl alloy layer.

The presence of Mg imparts an additional effect on the composition of the surface oxide layer. By taking the difference in the formation energy of MgO and Al_2O_3 into account, the reduction of Al_2O_3 by Mg is possible, as shown in Eq. [1]:

$$Al_2O_3 + 3Mg \rightarrow 2Al + 3MgO \qquad \Delta G = -344.98 \text{ kJ/mol} \qquad [1]$$

This reaction may account for the rather continuous interface between the outer oxide layer (ZnO + MgO) and the inner oxide layer where Al species are mainly present. This is different from the gaps between the outer Zn oxide and the inner Al oxide commonly observed in the GI steels after austenitization.[6,23,38]

The austenitization treatment slightly influences the difference in the corrosion potential between the coating and the steel substrate, that is, 0.563 V_{SCE} and 0.548 V_{SCE} for the as-received and austenitized 11Al-3Mg-Zn-coated steel, respectively. Nevertheless, the lowest potential plateau lasts for approximately 2450 seconds for the as-received, 11Al-3Mg-Zn-coated steel but only around 250 seconds for the austenitized counterpart. As a result, the as-received steel can provide larger degrees of cathodic protection than the austenitized counterpart can. This is consistent with the fact that the 11Al-3Mg-Zn coating has superior corrosion resistance compared with commercial GI and GA coatings, as evaluated by the salt spray test and electrochemical tests.[57–60] When most Al and Mg in the 11Al-3Mg-Zn melt are repelled to the interface and surface, respectively, the oxidation is markedly avoided. Nevertheless, the nearly-pure Zn major layer undergoes a fast dissolution in the corrosion test solution because of the lack of the formation of stable corrosion products. The cathodic protection efficiency of the 11Al-3Mg-Zn-coated steel is thus reduced after austenitization.

LMIE happens when there is liquid Zn(Fe) coexisting with α-Fe(Zn) and sufficient high stresses are applied to induce an direct contact of liquid Zn(Fe) with the steel substrate.[36,37] Previous studies on Al-Si coatings on boron steels have shown that the Fe-Al phase layer in between the coating and the substrate can restrain the cracks from extending.[9,11–13] How the polygonal crystal layer composed of Fe-Al phases influences the LMIE behaviors is thus worthy of further study. Several studies have indicated that the primary variable to design effective Zn-based coatings for hot stamping application is the thickness of the coating.[36,37] In this present study, the 11Al-3Mg-Zn-coated steel is for practical applications such as architectures and constructions. Considering the atmospheric corrosion protection, the thickness of the 11Al-3Mg-Zn coating is controlled to be within 20 to 30 μm to ensure sufficient corrosion protection.

The ideal microstructure of the Zn-based coating on steel after austenitization should consider (1) a thin oxide layer mainly composed of MgO and Al_2O_3; (2) a Zn layer with proper thickness to impart sufficient cathodic protection; and (3) a continuous FeAl layer with enough thickness to avoid the LMIE. The results of the present study can provide a basis for designing a Zn-Mg-Al ternary coating through composition and

thickness control for the application as a protective coating for press-hardening steels.

V. CONCLUSIONS

This study investigated the microstructure evolution of 11Al-3Mg-Zn coating on steels. The key findings are summarized as followings:

(1) The 11Al-3Mg-Zn coating undergoes obvious phase transformation after 5 minutes of austenitization at 1173 K (900 °C). The resulting coating consists of a Fe-Al alloy layer at the interface, a nearly pure Zn layer as the major layer, and a thin oxide layer mainly composed of MgO and ZnO.
(2) The oxide layer prevents oxidation and evaporation of molten Zn and the presence of the Fe-Al alloy layer retards the formation of Fe-Zn intermetallic compounds. Both contributes to the preservation of Zn in the coating.
(3) The presence of Mg promotes the formation of a stable oxide layer on the surface of the molten Zn.
(4) The nearly pure Zn layer affords a cathodic protection over the steel substrate. Nevertheless, its protection is inferior to the as-received 11Al-3Mg-Zn coating.

ACKNOWLEDGMENTS

The authors are grateful to the Ministry of Science and Technology of Taiwan for the financial support under Grant MOST 104-2622-8-006-001.

REFERENCES

1. R. Kuziak, R. Kawalla, and S. Waengler: *Arch. Civ. Mech. Eng.*, 2008, vol. 8, pp. 103–17.
2. J. Galan Lopez, L. Samek, P. Verleysen, K. Verbeken, and Y. Houbaert: *Rev. Metall.*, 2012, vol. 48, pp. 118–31.
3. D.W. Fan, H.S. Kim, and B.C. De Cooman: *Steel Res. Int.*, 2009, vol. 80, pp. 241–48.
4. H. Karbasian and A.E. Tekkaya: *J. Mater. Process. Technol.*, 2010, vol. 210, pp. 2103–18.
5. C. E. Ridderstråle: Patent GB1490535, Sweden, 1977.
6. D.W. Fan and B.C. De Cooman: *Steel Res. Int.*, 2012, vol. 83, pp. 412–33.
7. K. Mori and D. Ito: *CIRP Ann.-Manuf. Technol.*, 2009, vol. 58, pp. 267–70.
8. J. Kondratiuk, P. Kuhn, E. Labrenz, and C. Bischoff: *Surf. Coat. Technol.*, 2011, vol. 205, pp. 4141–53.
9. D.W. Fan and B.C. De Cooman: *ISIJ Int.*, 2010, vol. 50, pp. 1713–18.
10. L. Dosdat, J. Petitjean, T. Vietoris, and O. Clauzeau: *Steel Res. Int.*, 2011, vol. 82, pp. 726–33.
11. M. Windmann, A. Röttger, and W. Theisen: *Surf. Coat. Technol.*, 2014, vol. 246, pp. 17–25.
12. Z.X. Gui, K. Wang, Y.S. Zhang, and B. Zhu: *Appl. Surf. Sci.*, 2014, vol. 316, pp. 595–603.
13. K. Uda, A. Azushima, and A. Yanagida: *J. Mater. Process. Technol.*, 2016, vol. 228, pp. 112–16.
14. W.J. Cheng and C.J. Wang: *Surf. Coat. Technol.*, 2009, vol. 204, pp. 824–28.
15. Z.X. Gui, W.K. Liang, Y. Liu, and Y.S. Zhang: *Mater. Des.*, 2014, vol. 60, pp. 26–33.
16. W.J. Cheng and C.J. Wang: *Appl. Surf. Sci.*, 2013, vol. 274, pp. 258–65.
17. C. Allély, L. Dosdat, L.O. Clauzeau, K. Ogle, and P. Volovitch: *Surf. Coat. Technol.*, 2014, vol. 238, pp. 188–96.
18. M. Windmann, A. Röttger, and W. Theisen: *Surf. Coat. Technol.*, 2013, vol. 226, pp. 130–39.
19. C.E. Jordan, K.M. Goggins, A.O. Benscoter, and A.R. Marder: *Mater. Charact.*, 1993, vol. 31, pp. 107–14.
20. J. Mackowiak and N.R. Short: *Int. Met. Rev.*, 1979, vol. 24, pp. 1–19.
21. C.W. Lee, D.W. Fan, I.R. Sohn, S.J. Lee, and B.C. De Cooman: *Metall. Mater. Trans. A*, 2012, vol. 43A, pp. 5122–27.
22. C.W. Lee, W.S. Choi, L. Cho, Y.R. Cho, and B.C. De Cooman: *ISIJ Int.*, 2015, vol. 55, pp. 264–71.
23. R. Autengruber, G. Luckeneder, S. Kolnberger, J. Faderl, and A.W. Hassel: *Steel Res. Int.*, 2012, vol. 83, pp. 1005–11.
24. R. Mutschler, G. Thomas, P. V. Janavicius, and L. G. Garza-Martinez: Patent EP2997173A1, USA, 2014.
25. P. Fernandes and D. Jones: *Int. Mater. Rev.*, 1997, vol. 42, pp. 251–61.
26. L. Cho, H. Kang, C. Lee, and B.C. De Cooman: *Scripta Mater.*, 2014, vol. 90, pp. 25–28.
27. R. Autengruber, G. Luckeneder, and A.W. Hassel: *Corros. Sci.*, 2012, vol. 63, pp. 12–19.
28. H.H. Lee and D. Hiam: *Corrosion*, 1989, vol. 45, pp. 852–56.
29. E. Diler, B. Rouvellou, S. Rioual, B. Lescop, G.N. Vien, and D. Thierry: *Corros. Sci.*, 2014, vol. 87, pp. 111–17.
30. S. Schuerz, M. Fleischanderl, G. Luckeneder, K. Preis, K.T. Haunschmied, G. Mori, and A. Kneissl: *Corros. Sci.*, 2009, vol. 51, pp. 2355–63.
31. K. Honda, W. Yamada, and K. Ushioda: *Metall. Mater. Trans. A*, 2008, vol. 49A, pp. 1395–1400.
32. T. Prosek, N. Larché, M. Vlot, F. Goodwin, and D. Thierry: *Mater. Corros.*, 2010, vol. 61, pp. 412–20.
33. K.C. Yu, J. Li, X. Liu, J.G. Li, and X.H. Xue: *J. Shanghai Jiaotong Univ.*, 2012, vol. 17, pp. 663–67.
34. Y. Chen, Y. Liu, H. Tu, C. Wu, X. Su, and J. Wang: *Surf. Coat. Technol.*, 2015, vol. 275, pp. 90–97.
35. A. Marder: *Prog. Mater. Sci.*, 2000, vol. 45, pp. 191–271.
36. C.W. Lee and B.C. De Cooman: *Metall. Mater. Trans. A*, 2014, vol. 45A, pp. 4499–4509.
37. C.W. Lee, W.S. Choi, Y.R. Cho, and B.C. De Cooman: *Surf. Coat. Technol.*, 2015, vol. 281, pp. 35–43.
38. C.W. Lee, W.S. Choi, Y.R. Cho, and B.C. De Cooman: *ISIJ Int.*, 2014, vol. 54, pp. 2364–68.
39. NIST X-ray photoelectron spectroscopy database (Measurement Services Division of the National Institute of Standards and Technology (NIST) Technology Services, 2012), https://srdata.nist.gov/xps/. Accessed September 15, 2012.
40. C. Wagner, W. Riggs, L. Davis, J. Moulder, and G. Muilenberg: *Handbook of X-ray Photoelectron Spectroscopy*, Perkin-Elmer Corporation: Eden Prairie, MN, 1979, pp. 74–80.
41. B.R. Strohmeier: *Surf. Sci. Spectra*, 1994, vol. 3, pp. 121–27.
42. J.S. Corneille, J.W. He, and D.W. Goodman: *Surf. Sci.*, 1994, vol. 306, pp. 269–78.
43. G. Mattogno, G. Righini, G. Montesperelli, and E. Traversa: *J. Mater. Res.*, 1994, vol. 9, pp. 1426–33.
44. G. Schön: *J. Electron Spectrosc. Relat. Phenom.*, 1973, vol. 2, pp. 75–86.
45. S.P. Kowalczyk, R.A. Pollak, F.R. McFeely, L. Ley, and D.A. Shirley: *Phys. Rev. B*, 1973, vol. 8, pp. 2387–91.
46. B.R. Strohmeier: *Surf. Sci. Spectra*, 1994, vol. 3, pp. 128–34.
47. A. Miller, F. McCluskey, and J.A. Taylor: *J. Vac. Sci. Technol. A*, 1991, vol. 9, pp. 1461–65.
48. K. Djebaili, Z. Mekhalif, A. Boumaza, and A. Djelloul: *J. Spectrosc.*, 2015, vol. 2015, pp. 1–16.
49. G. Gusmano, E. Montesperelli, A. Traversa, A. Bearzotti, G. Petrocco, A. d'Amico, and C. Di Natale: *Sens. Actuators, B*, 1992, vol. 7, pp. 460–63.
50. J.A. Taylor: *J. Vac. Sci. Technol. A*, 1982, vol. 20, pp. 751–55.

51. H. Baker: *ASM Handbook: Alloy Phase Diagrams*, 10th ed., ASM International, Materials Park, OH, 1990, pp. 2.44, 2.56, 2.206.
52. P. Villars, A. Prince, and H. Okamoto: *Handbook of Ternary Alloy Phase Diagrams*, ASM International, Materials Park, OH, 1995, pp. 3660–72.
53. C. Jordan and A. Marder: *J. Mater. Sci.*, 1997, vol. 32, pp. 5603–10.
54. P. Bicao, W. Jianhua, S. Xuping, L. Zhi, and Y. Fucheng: *Surf. Coat. Technol.*, 2008, vol. 202, pp. 1785–88.
55. K.O. Lin, P.W. Chu, C.S. Lin, and H.B. Chen: *Metall. Mater. Trans. A*, 2013, vol. 44A, pp. 2690–98.
56. D.R. Gaskel: *Introduction to the Thermodynamics of Materials*, CRC Press, Boca Raton, FL, 2008, pp. 305–467.
57. C.B. Carter and M.G. Norton: *Ceramic Materials: Science and Engineering*, Springer, New York, NY, 2007, pp. 603–04.
58. Y. Morimoto, K. Honda, K. Nishimura, S. Tanaka, A. Takahashi, H. Shindo, and M. Kurosaki: Nippon Steel Technical Report, Nippon Steel Corporation, Japan, TYO, January 2003.
59. Y. Morimoto, M. Kurosaki, K. Honda, K. Nishimura, S. Tanaka, A. Takahashi, and H. Shindo: *Tetsu-to-Hagane*, 2003, vol. 89, pp. 161–65.
60. N. Shimoda and Y. Kubo: Nippon Steel Technical Report, Nippon Steel Corporation, Japan, TYO, March 2015.